Journal of Materials Science: Materials in Electronics (2018) 29:17454–17462
https://doi.org/10.1007/s10854-018-9845-y

Effect of porous modification on the synthesis and photocatalytic activity of graphitic carbon nitride/carbon quantum dot nanocomposite

Jianhui Shi[1] · Shuting Feng[1] · Tian Chen[1] · Yuzhen Li[1]

Received: 15 May 2018 / Accepted: 8 August 2018 / Published online: 12 August 2018

Abstract
Metal-free graphitic carbon nitride (g-C_3N_4) and carbon quantum dots (CQDs) have a promising attention as to their superior photocatalytic activities and physicochemical properties. In the article, g-C_3N_4 and CQDs were connected effectively through porous modification of g-C_3N_4 by directly heating melamine hydrochlorid, which benefits to the enhancement of the composites' photocatalytic activity. The structures and morphologies of the photocatalysts were characterized by X-ray diffraction, transmission electron microscopy, Fourier transform infrared spectroscopy, N_2 adsorption–desorption, X-ray photoelectron spectroscopy, UV–Vis diffuse reflectance spectrum and photoluminescence spectroscopy. Meanwhile, the porous g-C_3N_4 and CQDs composite (pg-C_3N_4/CQDs) exhibited the improved photocatalytic activity for the degradation of RhB under visible light irradiation, which may be contributed three reasons: (1) pg-C_3N_4 has much higher surface area (~20 times) and more stronger photocatalytic oxidation capacity than that of g-C_3N_4; (2) as the electron-sinks, CQDs can improve the photogenerated electron–hole pair's separation; (3) CQDs can upconvert the light with wavelengths longer than 650 nm into the shorter wavelengths to increase light harvesting, while pg-C_3N_4 utilizes the light to degrade pollutants. In addition, the possible photocatalytic degraded mechanism was investigated in detail. This work will be useful for designing other CQDs-based photocatalysts and providing a promising approach to environmental purification.

1 Introduction

Wang et al. have reported that graphite carbon nitride (g-C_3N_4) as a type of metal-free semiconductor can produce hydrogen or oxygen by splitting water under visible light irradiation [1]. g-C_3N_4 has attracted more and more attention in the field of photocatalysis because of its excellent properties, such as stable physical and chemical properties, good photoelectric properties, and easy to be prepared in large range [2–6]. The optical band gap of g-C_3N_4 was measured to be 2.7 eV, which allows it to respond to the visible light. There was a strong covalent bond between carbon and nitrogen atoms in g-C_3N_4, so it was still stable under the light irradiation in the aqueous solution, even in the acid–base solutions [4].

However, the pure g-C_3N_4 also has some disadvantages, such as the fast recombination of photo-generated electron–hole pairs, the small specific surface area and the weak visible light absorption [7]. In order to overcome these shortcomings, a great deal of methods have been proposed. The construction of heterojunction photocatalyst is a very effective and important method, because it can not only avoid the recombination of photo-generated electron–hole pairs, but also broaden the spectrum response range [8, 9]. Many heterojunction photocatalysts based on carbon nitride have been constructed and exhibit excellent photocatalytic performance in the degradation of organic pollutants. Many heterojunction photocatalysts based on g-C_3N_4-based have been constructed and exhibit excellent photocatalytic performance in the degradation of organic pollutants, such as titanium dioxide [10–24]. Of course, doping g-C_3N_4 with some carbon materials can also improve its photoelectric properties and photocatalytic properties, such as grapheme [25, 26], carbon nanotubes [27, 28] and so on.

Electronic supplementary material The online version of this article (https://doi.org/10.1007/s10854-018-9845-y) contains supplementary material, which is available to authorized users.

✉ Jianhui Shi
shijianhui@tyut.edu.cn

[1] College of Environmental Science and Engineering, Taiyuan University of Technology, Taiyuan, People's Republic of China

Carbon quantum dots (CQDs), as a new type of carbon nanomaterials, have been widely used in the field of photocatalyst construction because of their excellent properties, such as high solubility in water, strong size effect, up-conversion fluorescence properties and good photoinduced electron transfer properties [29–31]. In order to improve the photocatalytic performance of semiconductor, many heterojunction photocatalysts based on CQDs have been constructed, such as ZnO [32], TiO_2 [33], Ag_3PO_4 [34]. The connection between CQDs and TiO_2 in the TiO_2/CQDs heterojunctions is mainly depended on the hydrogen bonds formed by the carboxyl and hydroxyl groups of the surface of CQDs and the hydroxyl groups on the TiO_2. However, the surface of g-C_3N_4 contains some hydrophobic groups, which can not be strongly linked with CQDs. It is difficult to construct a heterojunction based on g-C_3N_4 and CQDs. Therefore, the interaction between them needs to be further solved.

In this paper, we proposed a method of porous modification of g-C_3N_4 to realize the effective connection between g-C_3N_4 and CQDs. The heterojunction composites constructed by porous g-C_3N_4 and CQDs showed excellent photocatalytic activity in the degradation of RhB under visible light irradiation, and the doping 0.5 wt% CQDs composites exhibited the highest photocatalytic activity. In addition, the possible mechanism of photocatalytic degradation has been studied in detail. This work will also propose a new idea for designing other heterojunction photocatalysts based on CQDs.

2 Experimental section

2.1 Synthesis of g-C_3N_4 and pg-C_3N_4

g-C_3N_4 two-dimensional nanocompounds was obtained from the pyrolysis of melamine according to the previously reported literature [35]. Specifically, a certain amount of melamine was placed in a crucible with a lid, heated to 500 °C at a speed of 15 °C/min in the muffle furnace and kept for 2 h, and then further heated to 520 °C and kept for 2 h again. Finally, the samples were cooled to room temperature to obtain g-C_3N_4 materials.

The synthesis methods of porous g-C_3N_4 (pg-C_3N_4) and g-C_3N_4 were similar, except that the roasted melamine was replaced by melamine hydrochloride. Melamine hydrochloride was obtained by the reaction of hydrochloric acid with melamine. In details, a certain amount of melamine was dissolved in deionized water and boiled by heating, and then adding slowly some hydrochloric acid into the above solution and stirring strongly for half an hour to form a sticky mixture. Finally, the sticky mixture was placed in the oven and dried all night at 80 °C to obtain the melamine hydrochloride.

2.2 Synthesis of g-C_3N_4/CQDs and pg-C_3N_4/CQDs

The CQDs were synthesized by ultrasonic treatment of alkali solutions according to the previously reported literature [36]. Specifically, 0.05 mol of glucose was added to 50 mL of deionized water and stirred to form a transparent solution, and then adding 50 mL of sodium hydroxide solution (1 mol/L) in the above solution. The mixed solution was placed in a supersonic chamber to ultrasonic treatment for 7 h at room temperature. The pH of the above mixture was then adjusted to 7 by the adding of hydrochloric acid. Finally, the raw solution was dialyzed through the semi permeable membrane (MWCO 3000), and the transparent brown solution was the CQDs aqueous solution. It was placed in the refrigerator and stored at 4 °C.

Fabrication of g-C_3N_4/CQDs heterostructures: The g-C_3N_4/CQDs heterostructures were synthesized by a simple deposition. Specifically, 0.1 g of g-C_3N_4 was added to 50 mL of the above stored CQDs aqueous solution. The mixture reacts for 4 h at 90 °C through the oil bath reflux and then cooled to room temperature. The mixture was centrifuged and washed many times with the deionized water. And then it was dried all night at 60 °C in the oven to obtain the final g-C_3N_4/CQDs heterostructures.

Fabrication of pg-C_3N_4/CQDs heterostructures: The synthesis methods of pg-C_3N_4/CQDs and g-C_3N_4/CQDs were similar, except that the replacement of g-C_3N_4 with pg-C_3N_4.

The added contents of CQDs were 0.1 wt%, 0.2 wt%, 0.5 wt%, 2.0 wt%, and referred to as g-C_3N_4(pg-C_3N_4)/CQDs (0.1%, 0.2%, 0.5%, 2.0%), respectively.

2.3 Characterization

Powder XRD patterns of the composites were obtained on a Rigaku-Dmax 2500 diffractometer using Cu Ka radiation (Ka = 1.54059 Å). Transmission electron microscopy (TEM) was taken with a field-emission transmission electron microscope. The X-ray photoelectron spectra (XPS) were recorded on an ECSALAB 250 spectrometer. Nitrogen adsorption–desorption analysis was carried out at liquid nitrogen temperature (77 K) by a Micromeritics ASAP 2010M instrument. The specific surface areas were calculated by the Brunauer–Emmett–Teller (BET) method. UV–Vis diffuse reflection spectroscopy were performed on a Shimadzu UV-2450 spectrophotometer using $BaSO_4$ as the reference. The photocurrent and electrochemical impedance spectroscopy (EIS) were examined by an electrochemical system, using a conventional three-electrode cell. The PL spectra of the photocatalysts were detected using a spectrophotometer.

2.4 Photocatalytic experiments

The photocatalytic activity of the above prepared samples was evaluated by photocatalytic degradation of rhodamine B (RhB) under visible light irradiation. A 300 W Xe lamp with a 420 nm cutoff filter as the light source was placed at 20 cm away from RhB solution. In the specific photodegradation reaction, the photocatalyst of 0.1 g was added to the RhB solution (10 mg/L) of 10 mL. Before the light irradiation, the mixture was stirred in dark for 40 min to reach the adsorption equilibrium of rhodamine B on the photocatalyst. In the process of the degradation reaction under visible light irradiation, the photocatalytic degradation solution was extracted every 5 min and centrifugated to remove the photocatalyst. And then the concentration of RhB was measured at this time by determing the maximum absorption peak of RhB at 553 nm through a ultraviolet spectrophotometer.

2.5 Photoelectrochemical measurements

The photoelectrochemical performance was tested through a conventional system. Typically, the measured sample electrode was used as the working electrode. And the platinum wire was used as the counter electrode and the Ag/AgCl electrode was used as the reference electrode. The photoelectrochemical measurements light source is a 300 W Xe lamp.

3 Results and discussion

3.1 Structural characterization of g-C_3N_4/CQDs composites

The crystal structure of the samples has been becharacterized by X-ray diffractometer (Fig. 1a, b). As shown in Fig. 1a, for the pure g-C_3N_4, there are two diffraction peaks at 13.0° and 27.4°, and these two peaks can be attributed to (100) and (002) crystallographic plane of g-C_3N_4. The weaker diffraction peak at 13.0° is derived from the in-plane structural packing motif, and the stronger diffraction peak at 27.4° is arises from the interlayer stacking [37]. However, the two diffraction peaks of pg-C_3N_4 are weaker and wider than that of the pure g-C_3N_4, which indicates that the crystallinity of pg-C_3N_4 is not as high as that of the pure g-C_3N_4. According to the diffraction peak of (002) plane in XRD, the average crystallite sizes of g-C_3N_4 and pg-C_3N_4 are 7.1 and 2.7 nm by Scherrer's formula, respectively [38], which indicates that melamine hydrochloride instead of melamine can effectively avoid the growth of g-C_3N_4 crystallite in the synthesis process. When the CQDs was loaded on the surface of g-C_3N_4 and pg-C_3N_4, both the characteristic peaks of g-C_3N_4 and pg-C_3N_4 become more weaker. This point can be observed obviously in the enlarge part of Fig. 1b. Moreover, no obvious CQDs diffraction peaks are observed, which may be due to the small amounts, high dispersion and low crystallinity of CQDs in heterojunctions [39]. In addition, no other impurities peaks are detected, revealing that the as-prepared photocatalysts are pure phase.

The morphology and microstructure of the samples have been studied by TEM (Fig. 2). The g-C_3N_4 sample synthesized by melamine as a precursor is a two-dimensional sheet-like structure, and when the melamine was replaced with melamine hydrochloride, the obtained g-C_3N_4 keeps its two-dimensional sheet-like structure, and the surface has an obvious mesoporous structure of about 10 nm, which indicates that the pg-C_3N_4 sample has been successfully synthesized. After assembling CQDs on the surface of g-C_3N_4 and pg-C_3N_4, the g-C_3N_4/CQDs heterostructures retain a sheet-like morphology and the surface of g-C_3N_4 is distributed sporadically with a small amount of CQDs (Fig. 2c). However, the surface of pg-C_3N_4 is homogeneously covered with a layer of dense CQDs, which is beneficial to the enhancement of photocatalytic activity of composites (Fig. 2d). This is also the goal that this article wants to achieve, and the specific reasons could be porousification of g-C_3N_4 leads to more active sites for deposition of CQDs.

The effective connection between pg-C_3N_4 and CQDs was proved by the FT-IR and XPS results. Figure 3 gives the FT-IR spectra of the as-prepared samples. As can be seen from Fig. 3a, the vibrations at 1075 (C–O), 1397 (C–H),

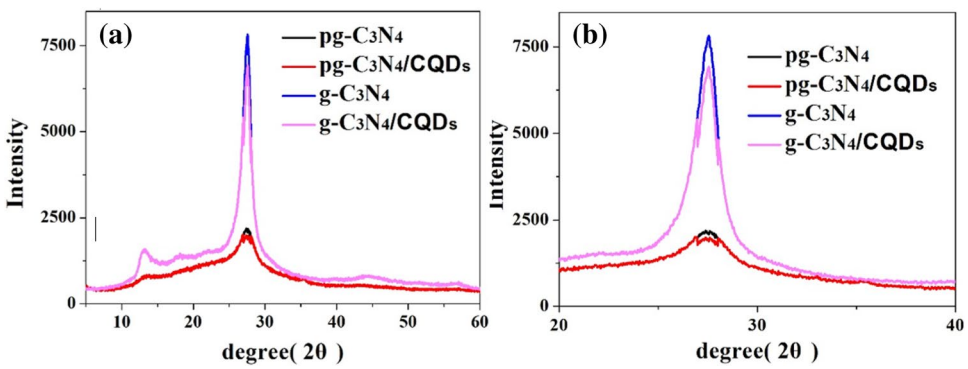

Fig. 1 XRD of patterns of **a** as prepared samples; **b** enlarged part of corresponding samples

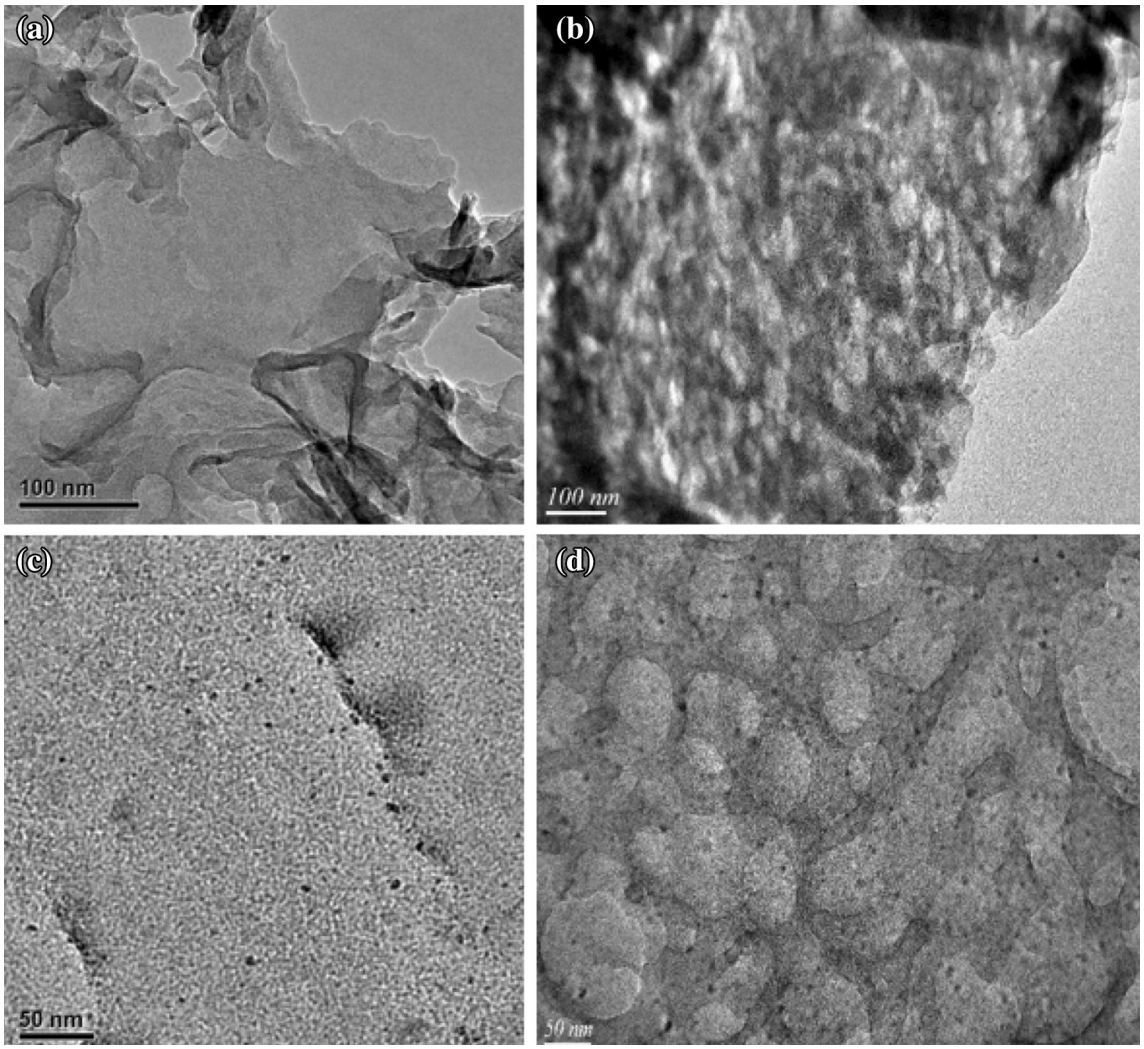

Fig. 2 TEM images of as-prepared samples: **a** g-C_3N_4; **b** pg-C_3N_4; **c** g-C_3N_4/CQDs; **d** pg-C_3N_4/CQDs

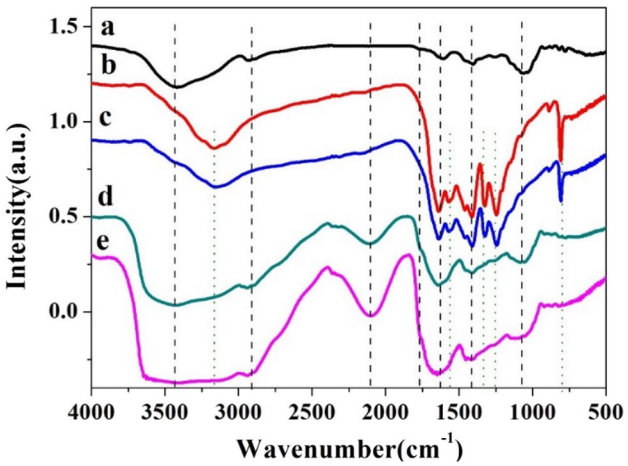

Fig. 3 FT-IR spectra of the samples: (*a*) CQDs; (*b*) g-C_3N_4; (*c*) pg-C_3N_4; (*d*) g-C_3N_4/CQDs; (*e*) pg-C_3N_4/CQDs

1645 (C=C), 1730 (C=O) cm^{-1} corresponding to carbon skeleton vibration are observed for CQDs. The broad bands at around 3400 cm^{-1} is assigned to the OH stretches due to adsorbed hydroxyl species. In Fig. 3b, the sharp absorption band at around 812 cm^{-1} could be assigned to the breathing mode of tri-s-triazine units [40]. The vibrations at 1635 (C=N), 1570 (C=N), 1456 (C–N), 1398 (C–N), 1319 (C–N) and 1248 cm^{-1} (C–N), corresponding to the typical stretching modes of CN heterocycles, comprising both N–$(C)_3$ and C–NH–C units. This indicated the formation of extended net-work of C–N–C bonds [41]. The broad bands at about 3200 cm^{-1} are indicative of stretching vibration modes for –NH of g-C_3N_4. For pg-C_3N_4, Fig. 3c shows the similar vibrations with g-C_3N_4, except for more weaker vibrations than that of g-C_3N_4, which indicated the successful porousification for g-C_3N_4. For Fig. 3d, e, there are the similar conditions that the characteristic vibrations of g-C_3N_4 (pg-C_3N_4) disappeared and the characteristic vibrations of

CQDs appeared. In addition, the vibration at 2100 cm^{-1} assigns to the conjugate vibrations between g-C_3N_4 (pg-C_3N_4) and CQDs, which reveals that the successful fabrication of g-C_3N_4 (pg-C_3N_4)/CQDs. Notably, all the vibrations of Fig. 3e are far stronger than that of Fig. 3d, it is due to pg-C_3N_4 has more active sites and active groups than g-C_3N_4, leading the deposition of more CQDs and more intimate connections with CQDs. The results are consist with the above TEM results.

XPS was used to further investigate the interactions between pg-C_3N_4 and CQDs (Fig. 4). The C 1s spectra of the pg-C_3N_4 can be fitted with two peaks at binding energies of 288.1 and 284.6 eV. The major peak at 288.1 eV is ascribed to the existence of sp^2-bonded C atoms C–N=C, while the peak at 284.6 eV is assigned to the existence of C=C. The two new peaks in pg-C_3N_4/CQDs composites are assign to C–OH (285.7 eV) and COOH (289.1 eV) species in CQDs [1]. The N 1s spectra of both pg-C_3N_4 and pg-C_3N_4/CQDs composites present the typical tertiary N–$(C)_3$ groups (400.5 eV) and C–N–C groups of triazine rings (398.4 eV) [42]. Interestingly, a new shoulder peak at 397.6 eV is obviously observed in pg-C_3N_4/CQDs composites, which may be caused by the intimate interaction between the pg-C_3N_4 and CQDs [43]. These results indicate that the the assembly of pg-C_3N_4/CQDs composites should be attributed to the $\prod$–$\prod$ stacking interaction between pg-C_3N_4 and CQDs. Such noncovalent interactions between the two components can prevent the formation of defects at the connection interface and thus lead to a intimate contact interface, which is also consistent with the TEM results.

In order to investigate the porous structure of samples, the nitrogen adsorption–desorption isotherms and Barret–Joyner–Halenda (BJH) pore size distribution curves of g-C_3N_4/CQDs and pg-C_3N_4/CQDs are given in Fig. 5. The results reveal that the two samples possess type III adsorption–desorption isotherms, which is caused by the weak adsorbent–adsorbent interaction and the porous structures of the sample. There are obviously type H_3 hysteresis loops

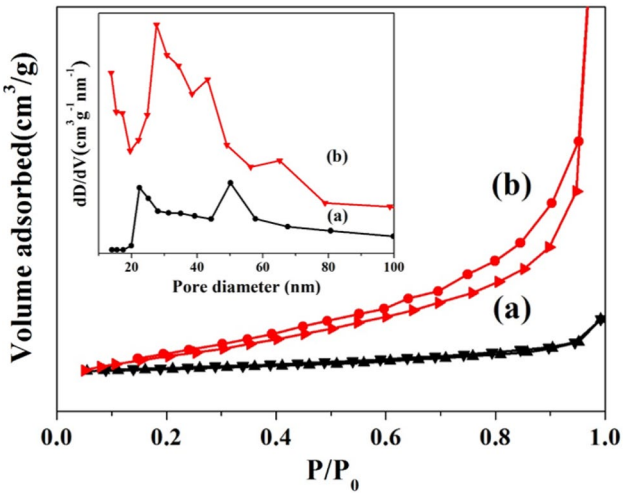

Fig. 5 N_2 adsorption–desorption isotherms and BJH pore size distribution plots (inset) of (*a*) g-C_3N_4/CQDs and (*b*) pg-C_3N_4/CQDs samples

at $0.50 < P/P_0 < 1.00$ in the isotherms of the pg-C_3N_4/CQDs sample, which can be often observed on the aggregates of plate-like particles lead to slit-shaped pores, confirming the existence of porous structure in pg-C_3N_4/CQDs. The BET specific surface areas of g-C_3N_4/CQDs and pg-C_3N_4/CQDs are calculated to be 2.8 and 57.7 m^2/g, respectively, suggesting that the utilization of melamine hydrochloride precursor could significantly increase the surface area of the final product by 20 times owing to the porousification of g-C_3N_4, which will be benefit to enhance the photocatalytic activity.

TEM image of the as-obtained CQDs is shown in Fig. 6a. The small CQDs are spherical particles with a diameter of approximate 5 nm and have good monodispersity. They can freely disperse in water with a transparent appearance (Fig. S1) due to the presence of hydrophilic groups on the surface, which was proved by the above FT-IR and XPS results.

Specially, the as-prepared CQDs shows the up-converted PL properties with excitation wavelengths at 650, 700,

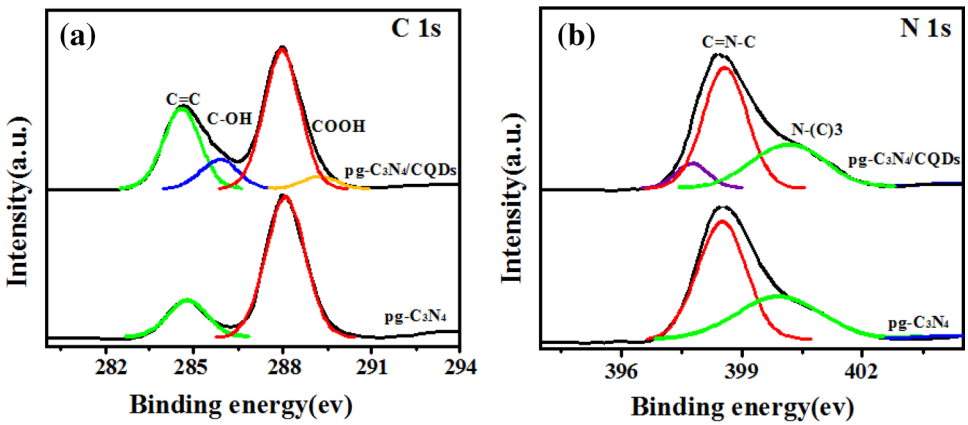

Fig. 4 XPS of C 1s (**a**) and N 1s (**b**) of pg-C_3N_4 and pg-C_3N_4/CQDs composites

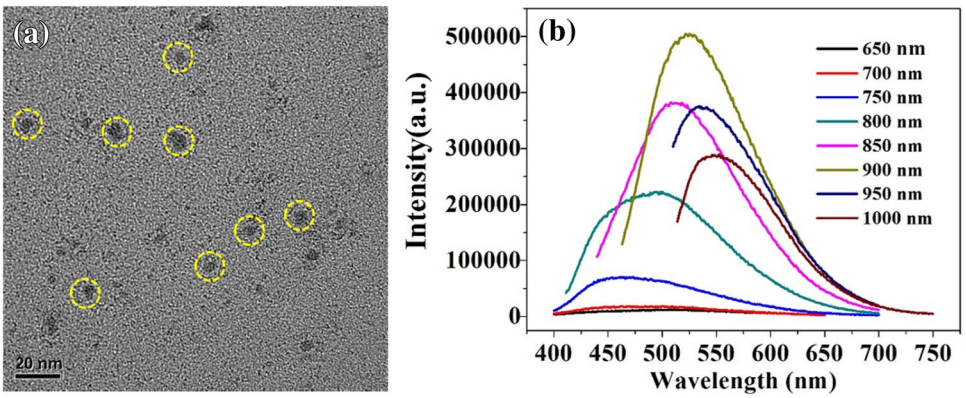

Fig. 6 **a** TEM images of CQDs; **b** up-converted photoluminescence spectra of CQDs

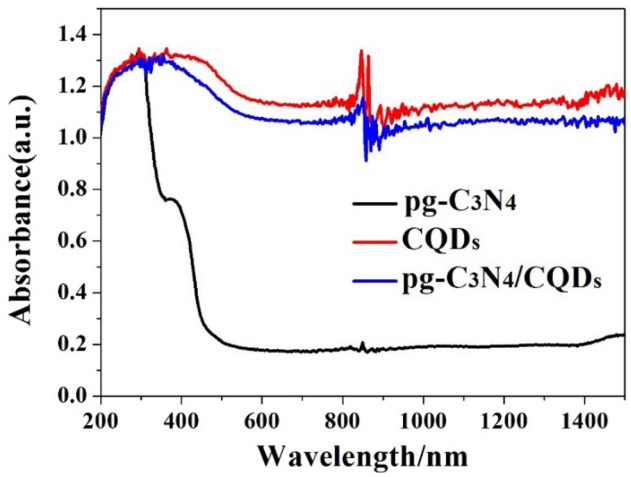

Fig. 7 UV–Vis–NIR absorption spectra of samples

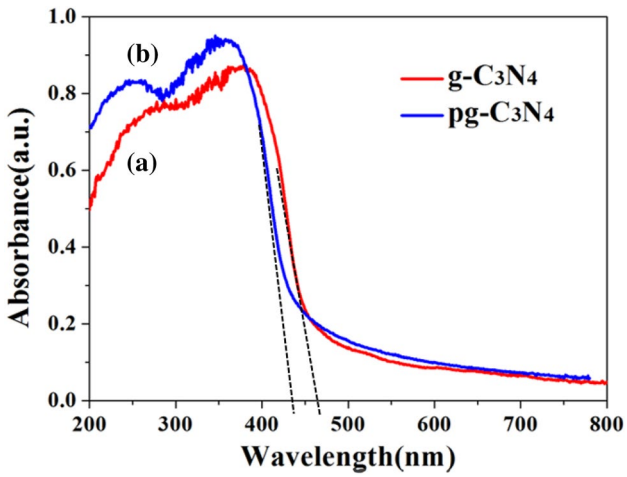

Fig. 8 UV–Vis diffuse reflectance spectra of (*a*) g-C_3N_4 and (*b*) pg-C_3N_4

750, 800, 850, 900, 950, and 1000 nm (NIR light region) (Fig. 6b). It is found that the emissions are located at visible light wavelengths of 400–600 nm. That is to say, CQDs can absorb NIR light and then emit visible light, which can in turn excite a visible-light photocatalyst to form electron–hole pairs, make the photocatalyst can effectively harness the broad spectrum of sunshine to strengthen the photocatalytic activities. This point is also proved by the results of UV–Vis–NIR absorption spectra of samples in Fig. 7. Pg-C_3N_4 shows strong absorption in the UV–Vis region, and the absorption wavelength is approximately 200–450 nm. While pg-C_3N_4/CQDs heterostructures also display obvious UV–Vis–NIR absorption ranging from 200 to 1400 nm. Compared to pg-C_3N_4, the large red shift of the heterostructure arises from the effective interaction between pg-C_3N_4 and CQDs. At the same time, this indicates the pg-C_3N_4/CQDs photocatalyst could harness solar energy more efficiently.

Figure 8 displays the UV–Vis diffuse reflectance spectra of as-prepared samples. It can be found that the pure g-C_3N_4 possesses absorption wavelength from the UV to the visible light region which can be up to around 460 nm, while the pg-C_3N_4 can be only up to 440 nm. For g-C_3N_4 and pg-C_3N_4, the calculated gaps are 2.70 and 2.81 eV respectively. It can be seen that the gap of g-C_3N_4 can be enlarged by 0.11 eV due to the porous modification of g-C_3N_4, which can enhance its photocatalytic oxidation capacity. We consider that the enlarged band gap of pg-C_3N_4 could be attributed to the quantum size effect due to their smaller crystal sizes [44]. After the introduction of CQDs on the surface of pg-C_3N_4, the absorption edge of pg-C_3N_4 did not shift, which indicates that the CQDs only deposite on the surface of pg-C_3N_4 and does not change its optical properties. The visible light harvesting capability of the pg-C_3N_4/CQDs composites increased with the CQDs content due to the intrinsic optical absorbance of the CQDs, which are confirmed in Fig. S2. Indeed, CQDs possesses the upconverted photoluminescence property as the results given in Fig. 6b. These results reveal that CQDs can serve as a light harvesting component for pg-C_3N_4/CQDs to improve visible light utilization, which enhance

the photocatalytic performance of the composites under sunlight.

3.2 Photocatalytic performance of samples

The photocatalytic performance of the samples was evaluated by RhB degradation experiments considering that RhB has been widely used to evaluate the photocatalytic activity of the photocatalyst as one of the model dye pollutants. The mixed solution was kept for 40 min in the dark to ensure the adsorption–desorption equilibrium between the photocatalyst and RhB prior to light irradiation. Figure 9a gives the photocatalytic activities of synthesized samples for degradation of RhB under visible-light. The results show that self-degradation of RhB is negligible and pg-C_3N_4 possesses much better activity than g-C_3N_4 on the degradation of RhB. Therefore, the porousification could enhance the g-C_3N_4's photocatalytic activity. However, the greatly enhanced RhB degradation is observed upon the introduction of CQDs onto pg-C_3N_4. After the light irradiation for 210 min, 80.2%, 85.6%, 100%, and 80.0% of RhB are photodegraded with increasing the CQDs content from 0.1 to 2.0 wt%, respectively. Notably, pg-C_3N_4/CQDs(0.5%) photocatalyst shows the highest RhB degradation rate. The results indicate that CQDs could enhance futher the photocatalytic activity of pg-C_3N_4, and the optimum amount of load is 0.5%. The more loading amounts of CQDs may cover the active sites of pg-C_3N_4, leading to the weaker photocatalytic activity of the pg-C_3N_4/CQDs composite.

Considering the importance of photocatalyst stability in practical applications, the photocatalytic reusability of the pg-C_3N_4/CQDs(0.5%) sample for RhB degradation was also evaluated. After each cycling photocatalytic experiment, the photocatalysts were collected, washed and dried for next recycling. From Fig. 9b, it can be seen that the pg-C_3N_4/CQDs(0.5%) sample exhibits the same photocatalytic degradation activity over five successive cycles for the degradation of RhB. The result suggests that the high-stability of the pg-C_3N_4/CQDs photocatalyst for its practical applications, which is also confirmed by the below XRD and TEM results. The XRD results show there is almost no difference before and after five cycles for the photodegradation of RhB (Fig. S3). At the same time, the TEM analysis displays that the distribution and density of CQDs on the surface of pg-C_3N_4 are indistinguishable from those of the unused sample (Fig. S4). The high-stability of the pg-C_3N_4/CQDs composites may be attributed to the close connetion between the two due to the porousification of g-C_3N_4.

3.3 Photocatalytic mechanism for the pg-C_3N_4/CQDs composites

To conclude the RhB degradation mechanism by the pg-C_3N_4/CQDs composite, the transient photocurrent responses of the g-C_3N_4, pg-C_3N_4 and pg-C_3N_4/CQDs composites were carried out to examine the charges generation and recombination behaviors in these photocatalytic systems in Fig. 10a. The reproducible photocurrent responses during the "on–off" irradiation cycles indicated the good stability of these photoelectrodes. Notably, the pg-C_3N_4/CQDs composite presents the highest the photocurrent density, about onefold and half and onefold enhancement than those of g-C_3N_4 and pg-C_3N_4 electrodes, which indicates that the introduction of CQDs resulted in pg-C_3N_4/CQDs has the lowest electrons and holes recombination rate. At the same time, the result further confirms there is an intimate connection between pg-C_3N_4 and CQDs.

To validate the improved charge transfer behaviors of the pg-C_3N_4/CQDs, the EIS Nynquist plots of the g-C_3N_4, pg-C_3N_4 and pg-C_3N_4/CQDs photoelectrodes are presented in

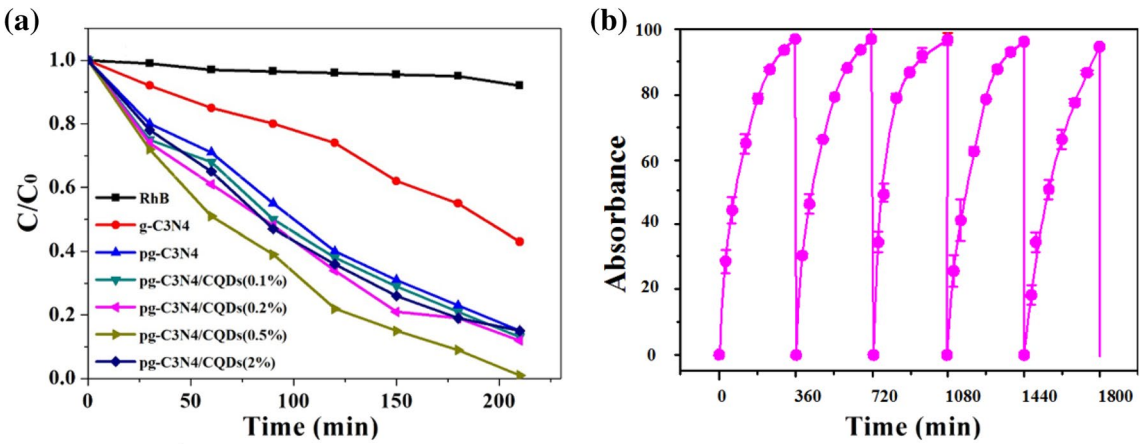

Fig. 9 **a** Photocatalytic degradation of RhB of as-prepared samples under visible-light; **b** cycling runs for the photodegradation of RhB of pg-C_3N_4/CQDs

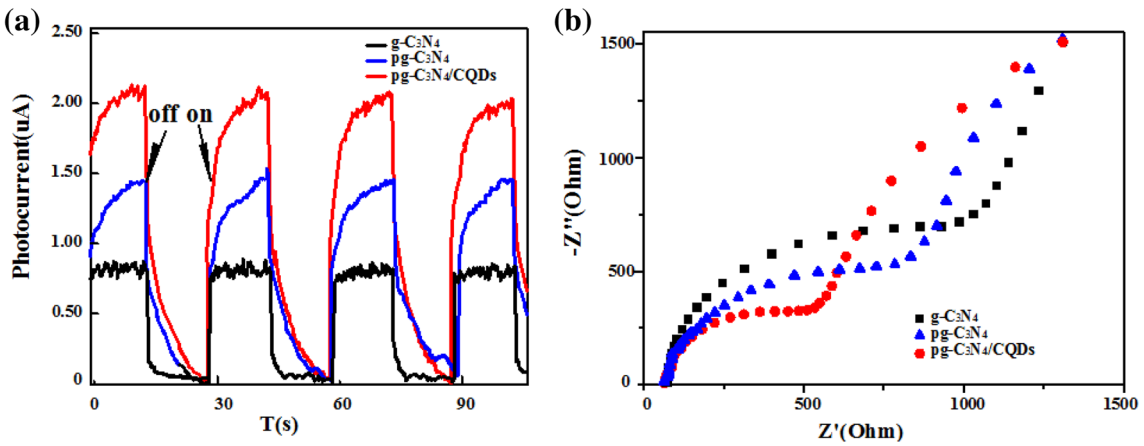

Fig. 10 **a** Photocurrent response curves and **b** EIS Nyquist plot of samples

Fig. 10b. As can be seen that the radius of three samples photoelectrodes are in the order of pg-C_3N_4/CQDs < pg-C_3N_4 < g-C_3N_4. It is well known that the smaller radius implies more efficient charges transfer process. Therefore, the results imply that charges transfer occurred more rapidly at the heterojunction interface of pg-C_3N_4/CQDs than that of g-C_3N_4 and pg-C_3N_4, which promotes efficient separation of the photogenerated electron–hole pairs. It is consistent with the result of transient photocurrent responses.

To investigate the photocatalytic mechanism for the pg-C_3N_4/CQDs composites, we had carried out RhB photodegradation experiments under the NIR light irradiation in Fig. S5. We can see that about 31% RhB are photodegradated over pg-C_3N_4/CQDs after 210 min. For RhB self-photolysis and pg-C_3N_4, there is no or little degradation of RhB is observed, which indicates pg-C_3N_4 photocatalysts do not respond to the NIR light. After CQDs deposited on the surface of pg-C_3N_4, the pg-C_3N_4/CQDs composites can respond to NIR light, leading to the photodegration of RhB under the NIR light irradiation. The results show that CQDs play the important roles for the enhanced NIR photocatalytic activity. As can be seen from Figs. 6b and 7, CQDs can harvest the NIR light and make it converted to visible light due to its up-conversion performance. As the result, the visible light excites pg-C_3N_4 to complete the NIR photocatalysis process in the pg-C_3N_4/CQDs composite.

Based on the above photocatalytic and photoelectrochemical results, a possible mechanism for the enhanced photocatalytic performance of the pg-C_3N_4/CQDs composite was proposed, which is illustrated in Fig. 11. Firstly, pg-C_3N_4 can be excited under the visible-light to yield photogenerated electron–hole pairs and electrons will migrate to the CQDs due to the intimate connection between pg-C_3N_4 and CQDs. Electrons on CQDs react with O_2 to form $^{\cdot}O_2^-$ that could oxidize RhB into CO_2 and H_2O. Meanwhile, the photogenerated h^+ can also directly oxidize RhB. Secondly, the light of the wavelength > 650 nm could be converted to < 550 nm light by CQDs owing to the up-converted PL behavior. Therefore, the pg-C_3N_4/CQDs composite could not only facilitate charges separation and transport at the junction interface through CQDs act as electron-sinks, but also promote more charges generation by extending the absorption

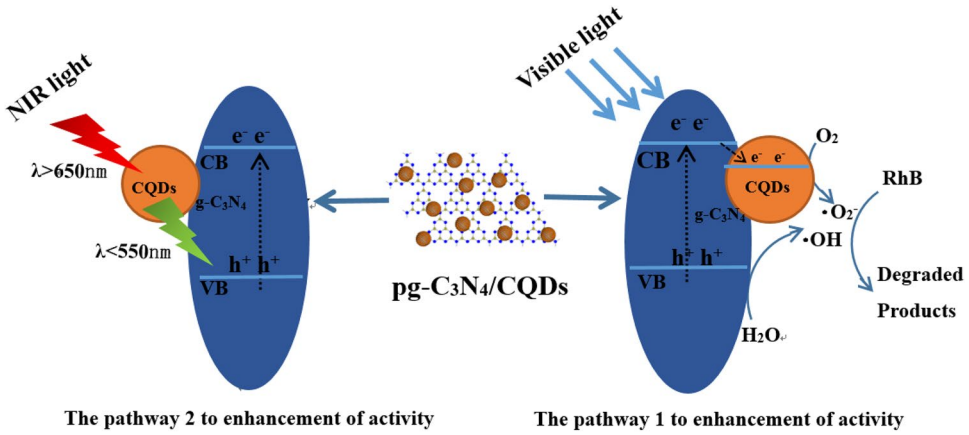

Fig. 11 Schematic diagrams for the possible photocatalytic mechanism of pg-C_3N_4/CQDs

region due to the up-converted performance of CQDs. The results lead to more efficient degradation of RhB under visible light irradiation.

4 Conclusions

In summary, the pg-C_3N_4/CQDs composites with the an intimate interface were successfully synthesized by the porous modification of g-C_3N_4. The photocatalytic activity of pg-C_3N_4 could be greatly improved by the deposition of CQDs on the surface of pg-C_3N_4, and the composites show the best photocatalytic activity as the loading amount of CQDs is 0.5%. The enhanced photocatalytic degraded mechanism of pg-C_3N_4/CQDs is investigated in detail, which could be contributed three reasons: (1) porous g-C_3N_4 has much higher surface area; (2) CQDs act as electron-sinks, which improve the photogenerated electron–hole pairs's separation; (3) CQDs act as the light source to up-convert infrared light to visible light to increase light harvesting. This work will be useful for designing other CQDs-based photocatalysts and providing a promising approach to environmental purification.

Acknowledgements This work was supported by Scientific and Technological Innovation Programs of Higher Education Institutions in Shanxi (Grant No. 2015128), and Qualified Personnel Foundation of Taiyuan University of Technology (QPFT) (Grant No. tyutrc-201326c) and the Shanxi Provincial Key Research and Development Plan (general) Social Development Project (Grant No. 201703D321009-5).

References

1. X.C. Wang, K. Maeda, A. Thomas, K. Takanabe, G. Xin, J.M. Carlsson, K. Domen, M. Antonietti, Nat. Mater. **8**, 76–80 (2009)
2. Z.W. Zhao, Y.J. Sun, F. Dong, Nanoscale **7**, 15–37 (2015)
3. S.W. Cao, J.G. Yu, J. Phys. Chem. Lett. **5**, 2101–2107 (2014)
4. S.W. Cao, J.X. Low, J.G. Yu, M. Jaroniec, Adv. Mater. **27**, 2150–2176 (2015)
5. K. Tian, W.J. Liu, H. Jiang, ACS Sustain. Chem. Eng. **3**, 269–276 (2015)
6. S.C. Yan, Z.S. Li, Z.G. Zou, Langmuir **26**, 3894–3901 (2010)
7. A.J. Du, S. Sanvito, Z. Li, D.W. Wang, Y. Jiao, T. Liao, Q. Sun, Y.H. Ng, Z.H. Zhu, J. Am. Chem. Soc. **134**, 4393–4397 (2012)
8. Y. Hou, F. Zuo, A. Dagg, P.Y. Feng, Nano Lett. **12**, 6464–6473 (2012)
9. Y.J. Wang, Q.S. Wang, X.Y. Zhan, F.M. Wang, M. Safdar, J. He, Nanoscale **5**, 8326–8339 (2013)
10. Z.W. Tong, D. Yang, T.X. Xiao, Y. Tian, Z.Y. Jiang, Chem. Eng. J. **260**, 117–125 (2015)
11. Z.A. Huang, Q. Sun, K.L. Lv, Z.H. Zhang, M. Li, B. Li, Appl. Catal. B **164**, 420–427 (2015)
12. J.Z. Li, Y. M, Z.F. Ye, M.J. Zhou, H.Q. Wang, C.C. Ma, D.D. Wang, P.W. Huo, Y.S. Yan, Appl. Catal. B **204**, 224–238 (2017)
13. T.T. Zhu, Y.H. Song, H.Y. Ji, Y.G. Xu, Y.X. Song, J.X. Xia, S. Yin, Y.P. Li, H. Xu, Q. Zhang, H.M. Li, Chem. Eng. J. **271**, 96–105 (2015)
14. W.L. Shi, F. Guo, J.B. Chen, G.B. Che, X. Lin, J. Alloys Compd. **612**, 143–148 (2014)
15. W.L. Yu, J.X. Chen, T.T. Shang, L.F. Chen, L. Gu, T.Y. Peng, Appl. Catal. B **219**, 693–704 (2017)
16. J. Di, J.X. Xia, M.X. Ji, B. Wang, S. Yin, H. Xu, Z.G. Chen, H.M. Li, Langmuir **32**, 2075–2084 (2016)
17. H.H. Wang, J. Lu, F.Q. Wang, W.H. Wei, Y. Chang, S.J. Dong, Ceram. Int. **40**, 9077–9086 (2014)
18. D.L. J, W.X. Ma, P. Xiao, D. Li, M. Chen, J. Colloid Interface Sci. **512**, 693–700 (2018)
19. M. Xiong, L. Chen, Q. Yuan, J. He, S.L. Luo, C.T. Au, S.F. Yin, Carbon **86**, 217–224 (2015)
20. G.Q. Tan, L.N. She, T. Liu, C. Xu, H.J. Ren, A. Xia, Appl. Catal. B **207**, 120–133 (2017)
21. M. Mitra, H.Y. Aziz, Adv. Powder Technol. **29**, 94–105 (2018)
22. Z. Zhu, Z.Y. Lu, D.D. Wang, X. Tang, Y.S. Yan, W.D. Shi, Y.S. Wang, N.L. Gao, X. Yao, H.J. Dong, Appl. Catal. B **182**, 115–122 (2016)
23. A. Mitra, P. Howli, D. Sen, B. Dasa, K.K. Chattopadhyay, Nanoscale **8**, 19099–19109 (2016)
24. Y.J. Yao, Y.M. Cai, F. Lu, J.C. Qin, F.Y. Wei, C. Xu, S.B. Wang, Ind. Eng. Chem. Res. **53**, 17294–17302 (2014)
25. Q. Han, N. Chen, J. Zhang, L.T. Qu, Mater. Horiz. **4**, 832–850 (2017)
26. W.J. Ong, L.L. Tan, S.P. Chai, S.T. Yong, A.R. Mohamed, Nano Energy **13**, 757–770 (2015)
27. Y. Zheng, L.H. Lin, B. Wang, X.C. Wang, Angew. Chem. Int. Ed. **54**, 12868–12884 (2015)
28. N. Wang, J. Li, L.P. Wu, X.J. Li, J. Shu, Int. J. Hydrog. Energy **41**, 22743–22750 (2016)
29. J. Liu, Y. Liu, N.Y. Liu, Y.Z. Han, X. Zhang, H. Huang, Y. Lifshitz, S.T. Lee, J. Zhong, Z.H. Kang, Science **347**, 970–974 (2015)
30. S.Y. Li, W. Shen, Z.Q. Gao, Chem. Soc. Rev. **44**, 362–381 (2015)
31. J.Z. Li, Y. Ma, Z.F. Ye, M.J. Zhou, H.Q. Wang, C.C. Ma, D.D. Wang, P.W. Huo, Y.S. Yan, Appl. Catal. B **204**, 224–238 (2017)
32. J. Wang, Z. Yang, X.X. Gao, W.Q. Yao, W.Q. Wei, X.J. Chen, R.L. Zong, Y.F. Zhu, Appl. Catal. B **217**, 169–180 (2017)
33. J. Tian, Y.H. Leng, Z.H. Zhao, Y. Xia, Y.H. Sang, P. Hao, J. Zhan, M.C. Li, H. Liu, Nano Energy **11**, 419–427 (2015)
34. M. Sun, Q. Zeng, X. Zhao, Y. Shao, P.G. Ji, C.Q. Wang, T. Yan, B. Du, J. Hazard. Mater. **339**, 9–21 (2017)
35. S.C. Yan, Z.S. Li, Z.G. Zou, Langmuir **26**, 3894–3910 (2010)
36. P.K. Harold, E.A. Leroy, *X-Ray Diffraction Procedures: For Polycrystalline and Amorphous Materials*, 2nd edn. (Wiley, New York, 1974)
37. X.J. Yu, J.J. Liu, Y.C. Yu, S.L. Zuo, B.S. Li, Carbon **68**, 718–724 (2014)
38. T.Y. Ma, S. Dai, M. Jaroniec, S.Z. Qiao, Angew. Chem. Int. Ed. **53**, 7281–7285 (2014)
39. W.J. Ong, L.L. Tan, S.P. Chai, S.T. Yong, Chem. Commun. **51**, 858–861 (2015)
40. S. Fang, Y. Xia, K.L. Lv, Q. Li, J. Sun, M. Li, Appl. Catal. B **185**, 225–232 (2016)
41. L. Zhao, F. Geng, F. Di, L.H. Guo, B. Wan, Y. Yang, H. Zhang, G. Sun, RSC Adv. **4**, 45768–45771 (2014)
42. S. Yang, X. Feng, X. Wang, K. Müllen, Angew. Chem. Int. Ed. **50**, 5339–5343 (2011)
43. J. Zhang, M. Zhang, L. Lin, X. Wang, Angew. Chem. Int. Ed. **54**, 6297–6301 (2015)
44. J.C. Yu, A.W. Xu, L.Z. Zhang, R.Q. Song, L. Wu, J. Phys. Chem. B **108**, 64–70 (2004)